Nanostructure and anisotropy of 3D printed lyotropic liquid crystals studied by scattering and birefringence imaging

Additive Manufacturing 47 (2021) 102289

Contents lists available at ScienceDirect

Additive Manufacturing

journal homepage: www.elsevier.com/locate/addma

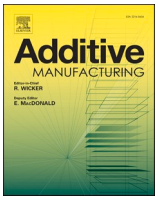

Research Paper

Nanostructure and anisotropy of 3D printed lyotropic liquid crystals studied by scattering and birefringence imaging

Adrian Rodriguez-Palomo [a,2], Viviane Lutz-Bueno [b,1,3], Manuel Guizar-Sicairos [b,4], Roland Kádár [c,5], Martin Andersson [d], Marianne Liebi [a,e,*,6,7]

[a] Department of Physics, Chalmers University of Technology, Gothenburg 41296, Sweden
[b] Swiss Light Source, Paul Scherrer Institute, Villigen PSI 5232, Switzerland
[c] Department of Industrial and Materials Science, Chalmers University of Technology, Gothenburg 41296, Sweden
[d] Department of Chemistry and Chemical Engineering, Chalmers University of Technology, Gothenburg 41296, Sweden
[e] Empa, Swiss Federal Laboratories for Materials Science and Technology, Centre for X-ray Analytics, St. Gallen 9014, Switzerland

ARTICLE INFO

Keywords:
Self-assembly
Lyotropic liquid crystals
3D printing
Scanning SAXS
Birefringence

ABSTRACT

Extrusion-based 3D printing of hexagonal and lamellar lyotropic liquid crystals is a powerful technique to produce hierarchical materials with well-defined anisotropic structure. Tailoring the properties of 3D printed objects requires a precise control of the nanostructure; however, a sufficiently high degree of anisotropy is often not achieved. In this study, scanning small angle X-ray scattering was performed *in situ* at the exit of the needle during 3D printing. We study the induced anisotropy and nanostructure in hexagonal and lamellar lyotropic liquid crystals. Mapping of extruded filaments during printing revealed that narrower nozzle diameters (370 μm) resulted in less anisotropic structures with a wider distribution of orientation angles across the cross section, while larger nozzle diameters (550 μm) resulted in more anisotropic structures with an overall higher degree of orientation. The apparent wall shear rate is higher for the narrower nozzle, which produces wall slip, resulting in a highly anisotropic shell, and a less aligned filament core. Further examination of the filaments revealed phase transitions due to solvent evaporation. The time scales were of 10–20 min of exposure to atmospheric conditions. Simultaneously, a loss in the macroscopic anisotropy of the hexagonal self-assembled structure was observed. These processes occur during and after extrusion-based 3D printing of liquid crystals and limit the fine control of the final structure. The variability of structures achieved for our different systems highlights the importance of structural characterization during and after extrusion to guarantee high anisotropy and well-defined structures.

1. Introduction

In additive manufacturing, also known as 3D printing, objects are manufactured layer-by-layer based on a Computer-Aided Design (CAD) model, thereby enabling the fast production of complex geometries. In addition, it does not require the use of molds or dies and does not generate excess waste material, thereby attracting attention from both the manufacturing industry and academia. In recent years, a wide variety of 3D printing methodologies have been developed, making it versatile and easily adaptable for future manufacturing [1]. For production of soft-matter, extrusion-based 3D printing is popular, which largely is due to the numerous options of extrudable materials [2,3].

Particularly, polymeric materials are used in extrusion-based 3D printing, due to the wide possibilities of crosslinking with e.g.

Abbreviations: H_1, self-assembled hexagonal phase; L_α, self-assembled lamellar phase; G', viscoelastic storage modulus; SAXS, small angle X-ray scattering.

* Corresponding author.
E-mail address: marianne.liebi@chalmers.se (M. Liebi).
[1] Current Address: Department of Health Sciences and Technology, ETH Zurich, Zurich 8093, Switzerland.
[2] ORCID: 0000-0002-5497-4914
[3] ORCID: 0000-0001-9735-5470
[4] ORCID: 0000-0002-8293-3634
[5] ORCID: 0000-0002-6255-4952
[6] ORCID: 0000-0003-1523-4697
[7] ORCID: 0000-0002-5403-0593

https://doi.org/10.1016/j.addma.2021.102289
Received 27 May 2021; Received in revised form 16 August 2021; Accepted 2 September 2021
Available online 11 September 2021

temperature [4], UV light [5], time [6], or sonication [7], as well as the opportunity to create complex functional systems. A wide variety of systems, including hydrogels, colloids and liquid crystals, have shown to be suitable materials for extrusion-based 3D printing intended for applications such as optically responsive devices [8], creation of composites with complex hierarchical structures [9], bio-inks capable to include living cells in their composition for tissue engineering [10] and designed for drug-delivery [11], among others.

For inks to be suitable for extrusion-based 3D printing, they should have well-controlled rheology, be designed for specific printing parameters and for a particular final application. The intrinsic properties of the material and its response to the imposed forces by the 3D printing setup and parameters will define the final structure and properties of the ink. It has been shown that inks having a non-Newtonian behavior with shear thinning and yield stress, such as silicon inks [12] and graphene oxide suspensions [13], are generally desired in 3D printing. The yield stress must be high enough so that the extruded filament and the final 3D object keeps its shape before crosslinking processes can be performed. However, high yield stresses might lead to clogging, or require high pressures. Therefore, low yield stresses with shear thinning behavior facilitate the flow through the nozzle. Furthermore, conditions for particle orientation during 3D printing have been assessed for cellulose nanocrystal suspensions, which rely on inducing stresses above the yield stress of the sample [14]. Particle orientation dynamics is determined based on the applied deformation rate and specific particle network interactions.

Among different inks, amphiphilic block co-polymers can assemble in ordered structures when they are in contact with a polar solvent. The hydrophobicity of certain blocks creates a segregation process, in which several blocks associate together to form an apolar domain while the hydrophilic block(s) create a polar domain. This leads to the creation of self-assembled structures such as spheres, bilayers, or cylinders [15], as schematically shown in Fig. 1a for cylinders and bilayers. Under certain conditions of temperature and polymer concentration in one or more solvents, these block co-polymers form lyotropic liquid crystals, which are made of repetitive self-assembled units with order in the long range in a well-defined crystalline lattices [16]. These lattices are highly dependent on the composition, which gives possibilities to study inks of different self-assembled structures for use in drug delivery [17] and as biomimetic composites [18], for example. A precise control of the anisotropy is an important requirement for the successful performance of hierarchical materials [19,20], optimizing the 3D printing process towards a high degree of orientation and uniformity across the strand is therefore needed. Controlling the anisotropy at the nanoscale enables the creation of hierarchical materials with well-defined anisotropic physical properties. These materials are of critical importance in heart valve replacements, where a fibrinous flexible tissue with anisotropic mechanical properties is needed [21], or to direct the mineralization process leading to an anisotropic mineralized composite [22].

Scattering techniques are appropriate to study the nanostructure and anisotropy of the intrinsic order of liquid crystals [23]. The use of small angle X-ray scattering (SAXS) is suitable since the building blocks of the

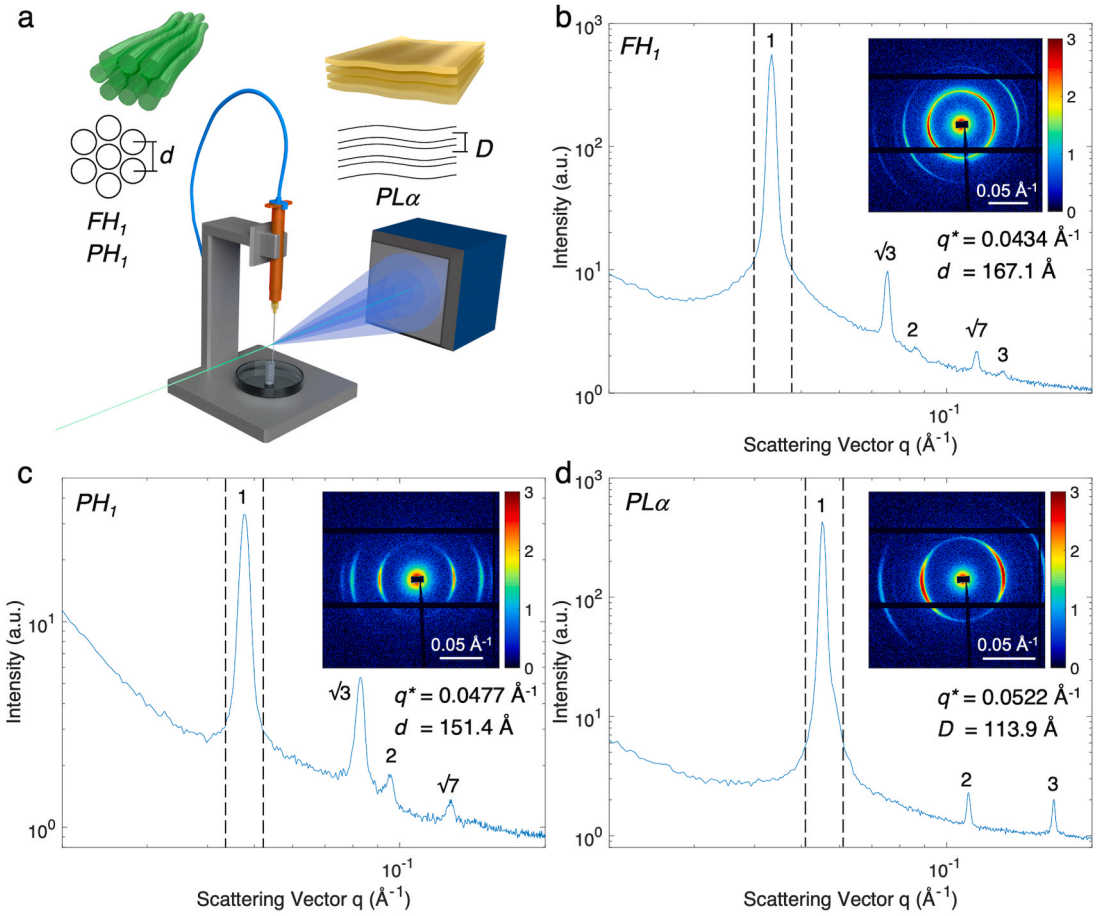

Fig. 1. a) Scheme of the self-assembled hexagonal and lamellar lyotropic liquid crystals and experimental set-up of the scanning SAXS experiment using *in situ* 3D printing. A 40 μm X-ray beam scans the extruded polymer and the scattering signal is recorded by a detector. Radial integration of the scattering signal for the polymer F in hexagonal self-assembled structure (b), P in hexagonal (c) and P in lamellar (d) printed with a 460 μm nozzle. The highlighted regions represent the selected *q*-range used in the calculations. A representative scattering pattern is shown as an example for each liquid crystal. *q** references the value of the main diffraction peak. The distance between cylinders (*d*) and lamella (*D*), respectively, is calculated from the main diffraction peak.

liquid crystals are in the range of tens of nanometers, and the created order produces a strong diffraction signal characteristic of each self-assembled structure. A focused beam enables the study of hierarchical 3D printed materials, allowing for spatial resolution in the macroscale by scanning the printed filament through the beam. In addition to scattering, the orientation in liquid crystals can be probed by monitoring changes in the polarization angle of light. The birefringence of polymers and macromolecules have two contributions; intrinsic and form birefringence [24]. The intrinsic birefringence is caused by the optical properties of molecules, whereas the form birefringence is caused by an anisotropic aggregate shape, such as cylinders or worm-like micelles [25]. In liquid crystals, isotropic phases, such as the cubic micellar phase, do not show birefringence, whereas hexagonal or lamellar phases typically show birefringence. However, not all anisotropic phases show a measurable birefringence, as the intrinsic and form birefringence can have opposing signs [26,27].

Control of macroscopic anisotropy is often desired since it affects electrical and thermal conductivity, optical properties, mechanical performance, or magnetic properties [28]. Anisotropy can be introduced by the shear and extensional forces during 3D printing which can reach relatively high alignment [29]. However, alignment using shear is limited to the printing direction and the shear forces created are limited by the nozzle diameter and flow rate in it [30]. This method, apart from reaching high degree of anisotropy, can be used to generate a specific texture in the nanostructure which could be used, for instance as templating to align particles [31]. However, knowledge to maximize the anisotropy and understand the source of the defects during and directly after printing is yet to be achieved. By combining SAXS and birefringence microscopy, we hereby aimed to visualize and explore the processes involved in the alignment of Pluronic based lyotropic liquid crystals in normal hexagonal and lamellar phase.

2. Materials and methods

2.1. Sample preparation

3D printable lyotropic liquid crystals were prepared by specific mixtures of polymer, water (milli-Q grade) and 1-butanol. The triblock co-polymer poly(ethylene oxide)-poly(propylene oxide)-poly(ethylene oxide) (PEO-PPO-PEO) was used with two different chain lengths, PEO_{100}-PPO_{70}-PEO_{100} (Pluronic© F-127), denoted as polymer *F* and PEO_{20}-PPO_{70}-PEO_{20} (Pluronic© P-123), denoted as polymer *P*. Hexagonal and lamellar self-assembled structures were prepared by controlling the weight ratio polymer:water:butanol [15], with hexagonal F-127 35:50:15, hexagonal P-123 45:55:0 and lamellar P-123 75:25:0, as shown in Table 1. The liquid crystals were vigorously mixed and left to equilibrate overnight. Subsequently, the liquid crystals were loaded in printing cartridges and centrifuged at 2.500 rpm for 10 min to remove possible air bubbles. Commercially available 3D printing cartridges were used with cylindric nozzles of 370 μm, 460 μm and 550 μm in diameter (CELLINK AB, Sweden). An air pressure controller (ElveFlow OB1 MK3+) was used to control the feed ratio to a constant value for all measurements.

2.2. Scanning SAXS

Scanning SAXS was performed at the coherent small-angle X-ray scattering (cSAXS) beamline at the Swiss Light Source (SLS) Paul Scherrer Institute (PSI, Switzerland). A focused X-ray beam of 40 × 40 μm was used with a photon energy of 11.2 keV (1.107 Å), selected by a fixed-exit double crystal Si(111) monochromator. The 3D printing cartridge and nozzle were mounted on a motorized stage with two degrees of freedom in the x-y plane, perpendicular to the beam, allowing to scan the 3D printed filament through the beam. A flight tube with a length of 2 m was placed between the sample and the detector to minimize air scattering and absorption. The scattering signal was recorded by a Pilatus 2 M detector [32] and the transmitted beam was measured with a photodiode on a beamstop inside the flight tube. The exposure time for all the *in situ* measurements was 0.08 s, at a sample-to-detector distance of 2.158 m, which was calibrated with silver behenate.

The scattering signal was azimuthally integrated and the phase of the liquid crystals identified by the ratio between the main diffraction peaks, corresponding to the distance between cylinders or bilayers in the crystals [15]. The angle of orientation and orientation parameter were calculated using the Hermans' Algorithm [33], which defines the Hermans' orientation parameter $\langle f_a \rangle$ as in Eq. (1), where $I(\phi)$ is the intensity for each azimuthal angle (ϕ) [34]. The Hermans' orientation parameter is a broadly used scalar order parameter, which defines the orientation of particle assemblies from X-ray scattering experiments using the intensity of the scattering over the azimuthal angle. The azimuthal intensity was normalized by its maximum intensity and interpolated using a Lorentzian curve. The angle of orientation was obtained by the peak position in the azimuthal intensity after the interpolation indicating the angle in real space, color-coded according to the displayed color-wheel.

$$\langle f_a \rangle = \frac{\int_0^{\pi} \left(\frac{3}{2}\cos^2\phi - \frac{1}{2}\right) \sin\phi \, I(\phi) \, d\phi}{\int_0^{\pi} \sin\phi \, I(\phi) \, d\phi} \quad (1)$$

The orientation parameter and angle of orientation in the scanning maps were averaged in the lowest 500 μm in order to avoid artifacts in the vicinity of the nozzle, such as instabilities and material expansion or contraction.

2.3. Birefringence microscopy

Spatially resolved retardance and angle of the optical fast axis were measured with the Exicor Birefringence MicroImager™ (Hinds Instruments, Inc., OR, USA). All measurements were performed with a LED source having a wavelength of 475 nm. The optical set-up consisted of a linear polarizer at 0°, a photoelastic modulator (PEM) at 45°, a PEM at 0° and a linear polarizer at 45°. The samples were placed in the sample stage between the two PEM and monitored with an objective of 20x (FH_1 and PH_1), which creates a field of view of 500 × 500 μm with a spatial resolution of about 0.25 μm/pixel. For the PL_α, the samples were imaged with a 10x objective which has a field of view of 1 × 1 mm and a spatial resolution of 0.50 μm/pixel. The microscope has a 2048 × 2048 pixel CCD camera. A stroboscopic light source was used to calculate the Mueller matrix components and provide quantitative measurements of the sample retardance and angle of the optical fast axis in the field of view [35,36]. The angle of the fast axis is color coded for easier interpretation.

Table 1
Description of the prepared samples including composition, self-assembled structure, and characteristic distance between cylinders (*d*) and lamellae (*D*).

Sample	Co-polymer	Polymer (%wt)	H2O (%wt)	1-butanol (%wt)	Self-assembled structure	Nanostructure spacing (Å)
FH_1	F-127	35	50	15	Hexagonal	167.1
PH_1	P-123	45	55	0	Hexagonal	151.4
PL_α	P-123	75	25	0	Lamellar	113.9

3. Results and discussion

3.1. Self-assembled nanostructure of the 3D printed filaments

Two different triblock co-polymers with the same block components, poly(ethylene oxide)-poly(propylene oxide)-poly(ethylene oxide) (PEO-PPO-PEO) but with different hydrophilic chain lengths were used in this study; polymer *F* with a block composition of $PEO_{100}PPO_{70}PEO_{100}$ and polymer *P* of $PEO_{20}PPO_{70}PEO_{20}$. Three different lyotropic liquid crystals were formed by adjusting the ratio between the polymer and the solvent (s) (see Materials and methods, Table 1). The resulting gels were extruded through a 3D printer cartridge mounted on motorized stages to scan the obtained filament through the X-ray beam, as schematically shown in Fig. 1a. Representative radial integration of the scattering signal for all the samples are shown in Fig. 1b-d. The obtained diffraction peaks proved that the materials had a mesoscopic order with two different self-assembled structures. For the liquid crystals made of polymer *F* with composition polymer:water:butanol 35:50:15 and *P* with 45:55:0, the diffraction peaks appear at the defined positions in the scattering vector *q* with a ratio of $1:\sqrt{3}:2:\sqrt{7}:3$ (Fig. 1b, c), which is characteristic for a normal hexagonal compact system (H_1). Those two samples were therefore labeled as FH_1 and PH_1, respectively. In a hexagonal phase, the polymer assembles in a cylindrical arrangement with the hydrophilic polyethylene chains facing the outer aqueous continues media and the middle hydrophobic polypropylene block facing the internal apolar domains. The cylinders are self-assembled in a hexagonal lattice with cylinder inter-distance of 167.1 Å and 151.4 Å for FH_1 and PH_1, respectively, as determined from the first diffraction peak. In the hexagonal phase, the aligned equally-spaced cylinders form an anisotropic scattering pattern, perpendicular to the long axis of the cylinders, i.e. in the direction of the alignment. The polymer *P* with composition 75:25:0 had the diffraction peaks at *q*-values with a ratio of 1:2:3 (Fig. 1d) characteristic for a lamellar structure (L_α) where the polymer form bilayers in a lamellar stack. This sample was denoted as PL_α, and had a lamellar distance of 113.9 Å. The lamellar phase also presents anisotropy in the scattering signal, where lamellae align parallel to the walls and in the direction of extrusion. The symmetry plane of the arcs is parallel to the lamella plane.

3.2. Macroscopic anisotropy of the 3D printed filaments

Fig. 2 summarizes the scanning SAXS results of the *in situ* 3D printing experiments, showing the Hermans' orientation parameter [33] $\langle f_a \rangle$ on the left side and the angle of orientation in the right side of the map for three different inner nozzle diameters; 370 μm, 460 μm and 550 μm as indicated with the red line on top, which are expected to produce a cylindrical filament. The high viscosity of PH_1 did not allow for extrusion through the smallest nozzle diameter and therefore it is not displayed in the figure. Both hexagonal structures had a higher orientation parameter when extruded through a larger nozzle diameter, as shown in the grey scale representation of the scanning maps (Fig. 2). The mean orientation parameter had an increase of 30% for FH_1 and 38% for PH_1 from the smallest to the largest nozzle, which reach a value up to $\langle f_a \rangle^{FH_1} = 0.64 \pm 0.06$ and $\langle f_a \rangle^{PH_1} = 0.61 \pm 0.02$, respectively. The overall orientation parameter in the lamellar structure, PL_α, is in contrast not significantly influenced by the nozzle diameter, as observed in both the scanning map in Fig. 2f-h as well as in Fig. 3, where each scanning line of the filament was radially averaged from the center in the lower 500 μm of the map.

Most filaments had a core-shell structure where the outer shell had a higher orientation parameter than the core of the filament. FH_1 had a core-shell structure for all three nozzles sizes, but the effect is less pronounced for the largest diameter (yellow stars in Fig. 3a) where the orientation parameter was found to be higher throughout the whole

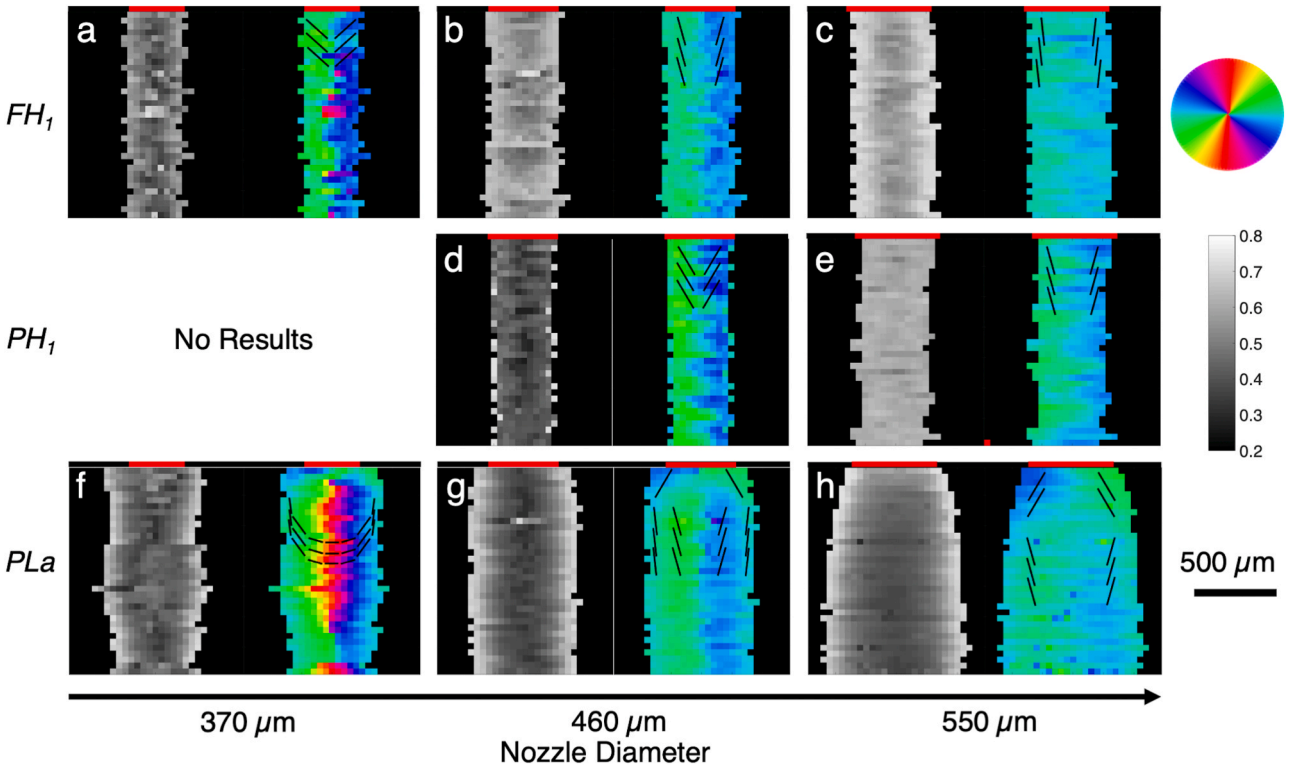

Fig. 2. Scanning SAXS of *in situ* 3D printed lyotropic liquid crystals. The printed strand was scanned using increasing nozzle diameters (left to right) for the three examined liquid crystals. The Hermans' orientation parameter (left side) and angle of orientation (right side) was calculated and color-coded for an easier interpretation. Black lines indicating the principal direction of alignment in the liquid crystals are added to the angle of orientation plots. The internal diameter of each nozzle is represented by a row of red pixels on the top of the scanning maps.

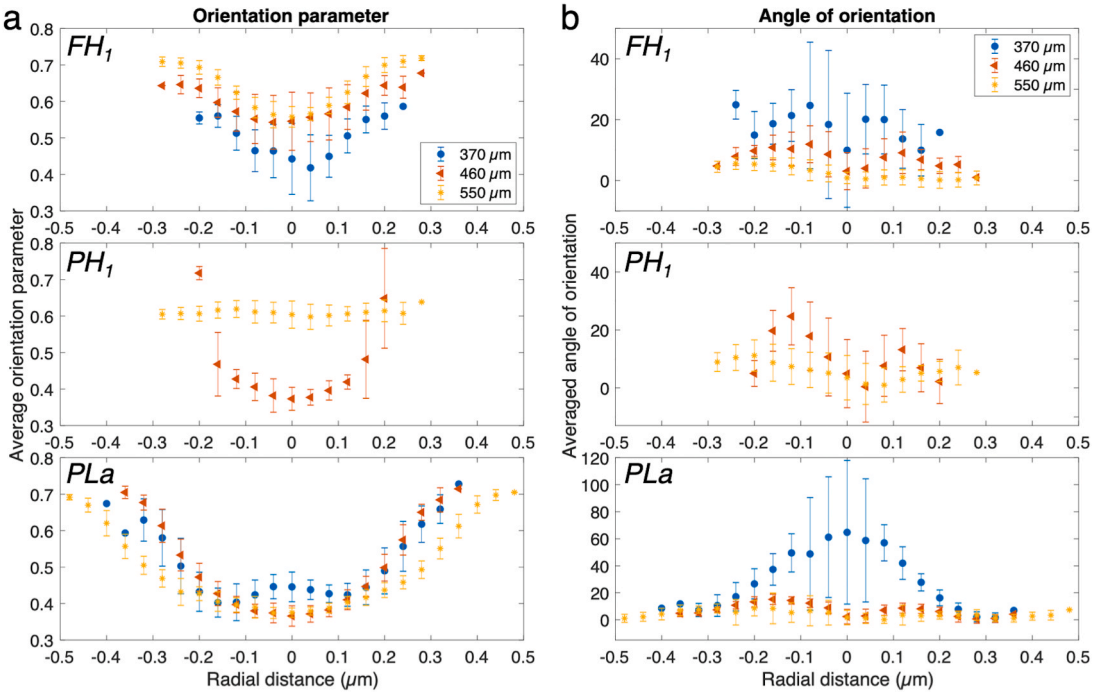

Fig. 3. Results for the average of the lowest 500 μm of each printed filament. Average values of the orientation parameter (a) and angle of orientation (b) including their variability calculated as the standard deviation. An angle of orientation of 0° represents alignment in direction of extrusion, the deviation is plotted in absolute values.

filament compared to smaller nozzle sizes. PH_1 exhibited a thin highly aligned shell (Fig. S2), when extruded through the 460 μm nozzle while becoming highly homogeneous when using the 550 μm nozzle (Figs. 2d-e and 3a). The bright pixels in PH_1 are indeed showing a highly oriented hexagonal phase and is not due to an effect of the edge scattering (see Fig. S2). The orientation parameter in the lamellar structure, PL_α has a more gradual change from the core to the shell, but is not significantly influenced by the nozzle diameter, as observed in Fig. 3a.

The angle of orientation induced by extrusion during the 3D printing process is color-coded according to the color wheel and indicated by black lines shown in Fig. 2. The mean angle of the main scattering orientation is in the range ±5° in all cases, defining 0° in the filament axis (vertical direction). This corresponds to an orientation of hexagonally packed cylinders with their long axis in the direction of extrusion (Fig. 2a-e), and a stack of lamellae in a coaxial wrapping following the filament axis (Fig. 2f-h). It is important to mention that the orientation of the anisotropy observed in the lamellar phase is always perpendicular to the vector normal to the surface of the lamellae (director), commonly used to define the orientation of the lamellar structures. The variation of the angle of orientation across the filament is strongly dependent on the nozzle diameter (Fig. 2). In Fig. 3b, 0° corresponds to an orientation in the extrusion direction, the deviation from it plotted in absolute values to account for the radial symmetry. The filaments produced by the largest nozzle (550 μm) had a more homogeneous alignment in the extrusion direction (turquoise) for the three materials as also seen in Fig. 3b with an angle of orientation close to zero. Smaller nozzles created a distinct pattern of alignment where the nanostructures are directed diagonally downwards from each side of the wall (blue and green, respectively). The 460 μm nozzle created a rather abrupt change in the middle forming a V-shape, while for the smallest nozzle (370 μm), structures in perpendicular orientation to the extrusion direction (red/pink) are observed, in particular for the lamellar phase where the transition is rather smooth forming a U-shape (Figs. 2f and 3b PL_α – 370 μm). The diameter of the filaments produced by the hexagonal structures is very similar to the inner diameter of the nozzle indicated with the red line in Fig. 2, and no change in diameter is observed along the printing direction. However, the lamellar phase PL_α exhibits an expansion by 56 – 73% after the exit of the nozzle, creating a filament bigger than the inner diameter of the nozzle (Fig. S3). This has an effect on the nanostructure orientation as seen in Fig. 2f-h, which are in the first 150–400 μm pointing outwards before they reverse into the U- or V-shapes described above. The expansion was not related with any change in the nanostructure since no change in lamellar spacing could be observed in the scattering signal (see Fig. S4).

The core-shell structure can be explained by a higher local shear rate in the proximities of the walls than in the middle, which significantly influences the viscosity and the orientation parameter in lyotropic liquid crystals [37]. In addition, an apparent wall slip effect could be detected in the liquid crystals in simple shear flow for shear rates above $\dot{\gamma} = 0.01\ s^{-1}$. Wall slip could occur towards the end of the nozzle as the isotropic pressure approaches atmospheric pressure conditions. Wall slip is observed in fluids with a large yield stress such as highly concentrated suspensions, caused by large shear rates, which produces a highly oriented outer layer in the filament [38,39]. The internal unyielded core is then pushed by the surrounding material. Narrower nozzles increase the wall shear stress likely increasing the wall slip effect [40–43]. This has revealed itself in a three-zone velocity profile for 3D printing inks based on colloidal gels [44]. In the core of that filament, an unyielded gel moves at a constant velocity (plug flow). The additional swelling effect observed in the lamellar phase, PL_α, could be related with the absence or diminished presence of apparent slip. High wall shear stress creates a highly aligned layer that might relax producing a rearrangement and swelling of the filament. In summary, the viscoelasticity of the material plays a very important role in the homogeneity and influence of the printing nozzle diameter. The use of larger nozzle diameters achieved higher degree of anisotropy, i.e., higher orientation parameter and more homogeneous distribution of angles.

3.3. Time evolution of the anisotropy

The structure of inks containing volatile solvents is susceptible to evaporation during the manufacturing process. The evaporation may

change their properties due to change in composition, which is in the case of lyotropic liquid crystals crucial to define their self-assembled structure. To shed light on phase stability in an open environment, birefringence microscopy was performed on the 3D printed filaments, which were imaged directly after printing and over a period of 30 min with one capture per min. The filament was extruded in the vertical position through a nozzle with inner diameter of 460 μm and transferred immediately to a glass slide for imaging. The change in the optical anisotropy of the ordered polymeric structures made it possible to follow the evolution of the anisotropy with time [45]. This measurement is equivalent to the waiting time the filament remains on the printing surface before the object is completed and the structure is fixated by crosslinking.

Fig. 4 shows the angle of the optical fast axis of the 3D printed liquid crystals over time according to the displayed color wheel and the value, i.e. the darkness, scaled with the retardance (separated values of the angle and retardance are plotted in the Fig. S5). The optical fast axis of FH_1 in Fig. 4a has an orientation parallel to the printing direction (Fig. S5a), which is in agreement with the scanning SAXS experiments shown in Fig. 2a-c. A highly aligned filament is initially printed with low retardance (Fig. S5b) i.e., low optical anisotropy, which at first increases with time. After about 17 min, the macroscopic orientation is lost and the formation of microdomains is observed, starting with a few microdomains of different orientations before extending to the whole analyzed area. The formation of microdomains goes together with a decrease in the retardance after 20 min. The extrusion process through a nozzle increases the shear stress and fluid velocity considerably. The high stresses induced in the microstructure may eventually relax forming ordered microdomains with random orientations [46]. PH_1 in Fig. 4b, produced a filament with high anisotropy. A homogeneous angle of the fast axis and a high retardance is visible (Fig. S5c,d). The retardance decreases gradually in the first 4 min, presumably by the effect of evaporation and relaxation. Already in the first frame a distinct region appears in the outer layer of the filament, which grows in the first 5 min. A lower retardance and opposite angle than the core is observed. After 5 min, the retardance values reach a minimum and the intensity of the birefringence signal is too low to consider the measured angle of the optical fast axis as reliable. This new signal has a high similarity with the lamellar phase in PL_α (Fig. 4c). The birefringence signal of the lamellar phase aligned radially in the cylinder shows a very low retardance with a homogeneous angle equal to the observed signal after the transition in PH_1 (Fig. S5e,f). The values of the retardance are too low to consider the angle accurate. The low retardance value of the lamellar phase is contradicting the high orientation parameter measured with SAXS. Macromolecules forming a bilayer have in general a positive intrinsic birefringence [24], whereas the form birefringence of lamellar systems is dominated by the arrangement and lamella interspace and is negative [47]. Certain configurations produce an interaction between the intrinsic and form birefringence that cancel each other, giving a net value close to zero [26]. The opposing effect of intrinsic and form birefringence can also explain the variation of the retardance within the two hexagonal phases, for which the intrinsic birefringence for molecules perpendicular to the long axis can be expected to be negative, whereas the form birefringence of a cylinder is positive [27]. The form birefringence is influenced by the d-spacing which may change with evaporation.

3.4. Time evolution of the self-assembled nanostructure

In order to further investigate the observed changes in the birefringence over time, the scattering signal of 3D printed filament was collected *in situ*, scanning across the diameter of the filament through the x-ray beam at several time points and then averaged for each scan line. It should be noted that the environmental conditions, such as humidity, at the beamline during the SAXS experiments were different than in the birefringence microscope, thus the exact times are not

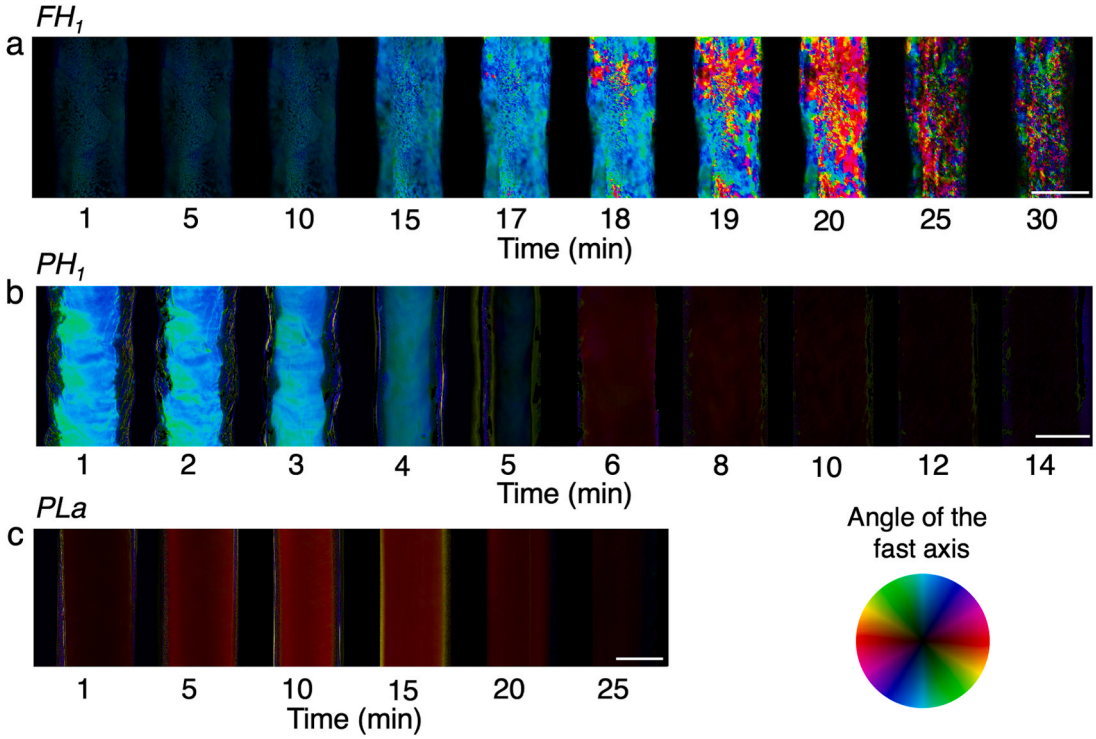

Fig. 4. Birefringence microscopy of the 3D printed liquid crystal over time with a nozzle of 460 μm in diameter. The combined plot with the angle of the optical fast axis is color coded according to the color wheel and the value scaled with the retardance. The separated colormaps showing the angle and retardance can be found in the Supporting Information (Fig. S5). The filament was 3D printed in the vertical axis and deposited on a glass slide in atmospheric conditions for the measurement. The time points, indicated in min, with most significant changes were selected to visualize the evolution. The background (glass slide) was masked. The scale bar represents 400 μm.

comparable, but the same sequence can be expected. For FH_1 in Fig. 5a the initial peak ratio is 1:√3:2:√7, representative of a hexagonal self-assembled structure. The hexagonal fingerprint remains visible over time, but the peaks get broader and less pronounced. In addition, there is a second population at lower q-values with a broader peak width at a characteristic distance of 167.41 Å. This can be related to the ordered domains in random directions observed by birefringence microscopy, perhaps in the interspace between ordered domains. In contrast to the retardance, the orientation parameter of the scattering pattern stays constant, with only a minor trend toward lower values observed with time, as shown in Fig. S6. Fig. 5b shows the time evolution of PH_1 starting with the characteristic hexagonal peak ratio 1:√3:2:√7. The main peak from the plane (01) is shifted to larger q-values and the secondary and tertiary peaks faint. A new structure appears with a peak ratio of 1:2:3 characteristic for a lamellar structure. Since the experiment was performed in atmospheric conditions, we assume a change of composition due to the loss of components by evaporation, which results in a shift in the phase diagram [15]. According to the phase diagram the loss of water displaces the composition towards the stability field of the lamellar phase. This phase transition was also observed by a change in the birefringence signal matching the lamellar phase as seen in Fig. 4c. A decrease in the orientation parameter is also observed in Fig. S7, in this case following the decrease of the retardance (Figs. 4b and S5d). The evolution of the sample PL_α is shown in Fig. 5c. The initial structure is a lamellar stack with peak relationship 1:2:3. The effect of time and evaporation induced here a partial phase change with three prominent peaks appearing at low q-values. Together with the new peaks, a shoulder at low q appears which can be fitted with a form factor from a sphere in cubic arrangement with a radius of 136 Å (Fig. S8). Among the possible self-assembled arrangements of spherical micelles, a cubic structure with the space group Pm3n (8 micellar units per unit cell) is the most common structure observed in surfactants with low molecular weight [48]. As described by B. Svensson et al. [49], the assumption of two or even four micellar units per cubic cell, as in BCC and FCC, is incompatible with the estimations of the area of the polar-apolar interface. This assumption results in a lower area than the hexagonal self-assembled structures, which should be lower. The indexation of the diffraction peaks could presumably match the reflection of the crystalline planes (200), (210) and (211) as described in a similar system [49], however the reflection (110) is not present. This result suggests the coexistence of two phases, which evolve over time. The orientation parameter in the SAXS experiments does not significantly change, as seen in the scattering signal in Fig. S9. The phase diagrams represent the self-assembled phases for the given parameters in the thermodynamic equilibrium [15]. The performed experiments involving extrusion and quick environmental changes are far from the thermodynamic stability, which open the possibility for different phases to occur. The scattering signal was checked at different positions across the filament diameter (Figs. S5, S6 and S9). No significant changes were observed. The step size used in the scanning SAXS experiments does not allow to resolve small changes on the surface; however, it is visible using birefringence microscopy, as observed in Figs. 4 and S5. This finding brings attention to the fact that the structure must be checked after 3D printing and the fixation needs to occur at time scales smaller than any observed relaxation or phase change. The printing of large objects implies long times, in which the composition of the gels might change and therefore their structure. This could be counteracted by a controlled atmosphere during printing.

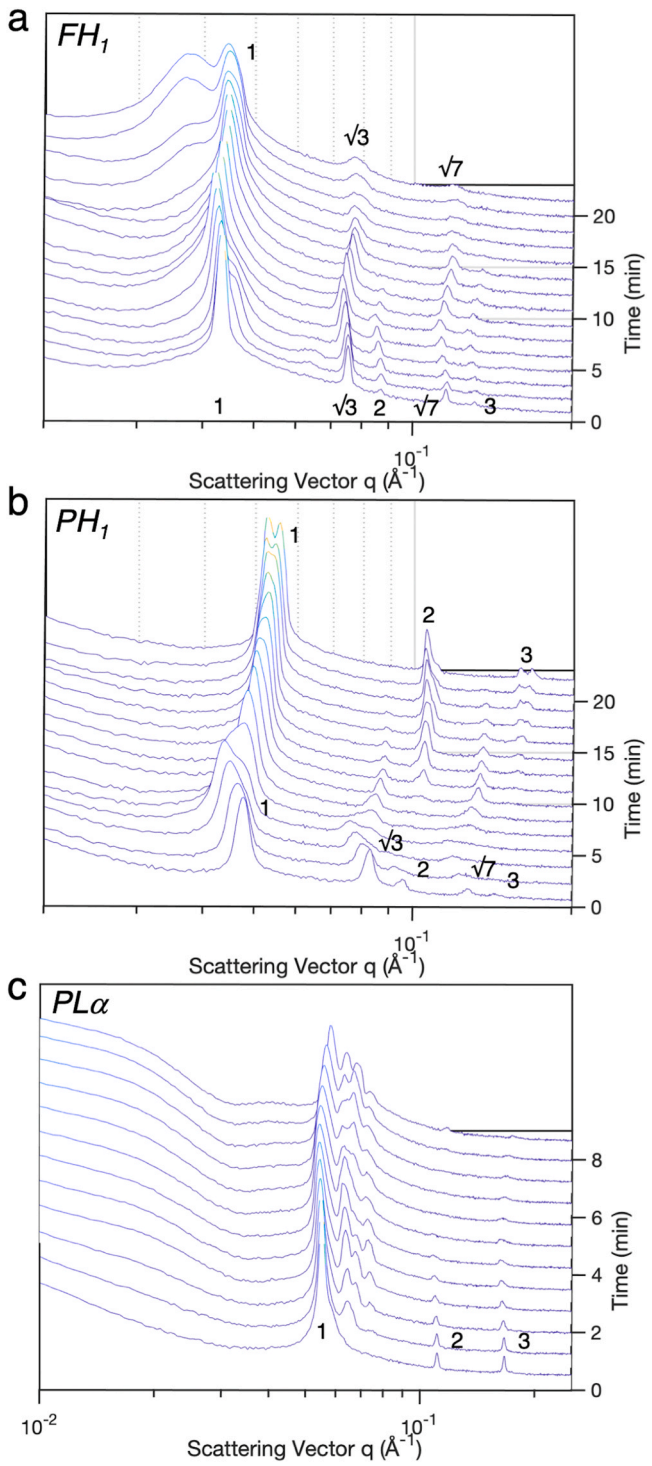

Fig. 5. Evolution of the azimuthally integrated SAXS signal from 3D printed liquid crystals over time for FH_1 (a), PH_1 (b) and PL_α (c). The extruded filament was scanned in the vertical position and the scattering signal was recorded in each point across the width. The evolution of the orientation parameter and scattering signal can be found in the Fig. S6, S7 and S9.

4. Conclusions

In this work, the anisotropy created by extrusion-based 3D printing was visualized *in situ* using scanning SAXS and birefringence microscopy. The angle of orientation and degree of anisotropy were measured in the aligned materials oriented in the flow direction. The general orientation of the structure was found to be in the printing direction. Surprisingly, a higher and more homogeneous orientation was achieved using larger nozzles. A core-shell structure was found in the orientation parameter with highly oriented outer layer and low oriented core. The use of smaller nozzles produced filaments with a wider distribution of angles, which make them less suitable for aligned filaments with controlled anisotropy.

The time evolution of the printed filament in ambient conditions was

tracked by SAXS and birefringence imaging concerning the self-assembled nanostructure and alignment. A general trend towards relaxation and disorder was observed after long exposure to ambient pressure and atmospheric conditions. The effect of evaporation led to a phase change from hexagonal to lamellar in the self-assembled hexagonal liquid crystal (PH_1) and to a phase coexistence between lamellar and cubic in the lamellar PL_α.

The orientation visualized with scanning SAXS and birefringence microscopy was qualitatively comparable in the hexagonal phases, the lamellar phase however did not show birefringence. The Hermans' orientation parameter and the retardance had qualitatively similar trends, while in the retardance additional effects from the phase transition play an important role. The complexity of these self-assembled materials makes a detailed study of the behavior of each individual structure necessary in order to avoid undesired secondary effects, such as the observed phase transitions and changes in the orientation. These findings point to the importance of a detailed observation of the nanostructure in self-assembled systems such as lyotropic or thermotropic liquid crystals, in which an uncontrolled change in the environmental conditions may lead to a change in the desired material and alter its performance.

CRediT authorship contribution statement

Adrian Rodriguez-Palomo: Conceptualization, Investigation, Formal analysis, Visualization, Writing – original draft. **Viviane Lutz-Bueno:** Investigation, Writing – review & editing. **Manuel Guizar-Sicairos:** Investigation, Software, Writing – review & editing. **Roland Kádár:** Resources, Investigation, Writing – review & editing. **Martin Andersson:** Resources, Supervision, Writing – review & editing. **Marianne Liebi:** Conceptualization, Resources, Investigation, Supervision, Funding acquisition, Writing – original draft.

Declaration of Competing Interest

The authors declare that they have no known competing financial interests or personal relationships that could have appeared to influence the work reported in this paper.

Acknowledgments

This work has been supported by the Area of Advance Material Science at Chalmers University of Technology and the Swedish Research Council (VR 2018–041449). The Wallenberg Wood Science Center (WWSC) and the Kristina Stenborg stiftelsen are acknowledged for financial support in acquisition of the birefringence microscope. This project has received funding from the European Union's Horizon 2020 research and innovation program under grant agreement No. 731019 (EUSMI). We acknowledge the Paul Scherrer Institute, Villigen, Switzerland for provision of synchrotron radiation beamtime at the beamline cSAXS of the SLS.

Author contribution

Adrian Rodriguez-Palomo and Marianne Liebi designed the idea of the experiment. Adrian Rodriguez-Palomo did the sample preparation and performed the scattering experiments together with Marianne Liebi, assisted by Viviane Lutz-Bueno and Manuel Guizar-Sicairos. The birefringence imaging was carried out by Adrian Rodriguez-Palomo as well as the rheology characterization, which was assisted by Roland Kádár. The data was analyzed by Adrian Rodriguez-Palomo with the assistance of Marianne Liebi regarding the scattering and Roland Kádár. regarding the rheology experiments. Adrian Rodriguez-Palomo prepared the manuscript and all the authors discussed the results and reviewed the manuscript. All authors have given approval to the final version of the manuscript.

Funding sources

Marianne Liebi and Adrian Rodriguez-Palomo have been supported by the Area of Advance Material Science at Chalmers University of Technology and the Swedish Research Council (VR 2018–041449) and the European Union's Horizon 2020 research and innovation program under grant agreement No 731019 (EUSMI).

Appendix A. Supporting information

Supplementary data associated with this article can be found in the online version at doi:10.1016/j.addma.2021.102289.

References

[1] R.L. Truby, J.A. Lewis, Printing soft matter in three dimensions, Nature 540 (7633) (2016) 371–378.
[2] L.-Y. Zhou, J. Fu, Y. He, A review of 3D printing technologies for soft polymer materials, Adv. Funct. Mater. 30 (28) (2020), 2000187.
[3] X. Wang, M. Jiang, Z. Zhou, J. Gou, D. Hui, 3D printing of polymer matrix composites: a review and prospective, Compos. Part B: Eng. 110 (2017) 442–458.
[4] J. Go, A.J. Hart, Fast desktop-scale extrusion additive manufacturing, Addit. Manuf. 18 (2017) 276–284.
[5] M. Müller, J. Becher, M. Schnabelrauch, M. Zenobi-Wong, Nanostructured Pluronic hydrogels as bioinks for 3D bioprinting, Biofabrication 7 (3) (2015), 035006.
[6] S.H. Ahn, H.J. Lee, J.-S. Lee, H. Yoon, W. Chun, G.H. Kim, A novel cell-printing method and its application to hepatogenic differentiation of human adipose stem cell-embedded mesh structures, Sci. Rep. 5 (1) (2015) 13427.
[7] S. Das, F. Pati, Y.-J. Choi, G. Rijal, J.-H. Shim, S.W. Kim, A.R. Ray, D.-W. Cho, S. Ghosh, Bioprintable, cell-laden silk fibroin–gelatin hydrogel supporting multilineage differentiation of stem cells for fabrication of three-dimensional tissue constructs, Acta Biomater. 11 (2015) 233–246.
[8] B.B. Patel, D.J. Walsh, D.H. Kim, J. Kwok, B. Lee, D. Guironnet, Y. Diao, Tunable structural color of bottlebrush block copolymers through direct-write 3D printing from solution, Sci. Adv. 6 (24) (2020) 7202.
[9] A.K. Rajasekharan, A. Lotsari, V. Lutz-Bueno, M. Liebi, M. Andersson, Bioinspired structural hierarchy within macroscopic volumes of synthetic composites, Adv. Healthc. Mater. 7 (18) (2018), 1800466.
[10] N. Beheshtizadeh, N. Lotfibakhshaiesh, Z. Pazhouhnia, M. Hoseinpour, M. Nafari, A review of 3D bio-printing for bone and skin tissue engineering: a commercial approach, J. Mater. Sci. 55 (9) (2020) 3729–3749.
[11] E. Mathew, G. Pitzanti, E. Larraneta, D.A. Lamprou, 3D printing of pharmaceuticals and drug delivery devices, Pharmaceutics 12 (3) (2020).
[12] M. Schaffner, J.A. Faber, L. Pianegonda, P.A. Rühs, F. Coulter, A.R. Studart, 3D printing of robotic soft actuators with programmable bioinspired architectures, Nat. Commun. 9 (1) (2018) 878.
[13] A. Corker, H.C.H. Ng, R.J. Poole, E. García-Tuñón, 3D printing with 2D colloids: designing rheology protocols to predict 'printability' of soft-materials, Soft Matter 15 (6) (2019) 1444–1456.
[14] M.K. Hausmann, P.A. Rühs, G. Siqueira, J. Läuger, R. Libanori, T. Zimmermann, A. R. Studart, Dynamics of cellulose nanocrystal alignment during 3D printing, ACS Nano 12 (7) (2018) 6926–6937.
[15] P. Holmqvist, P. Alexandridis, B. Lindman, Modification of the microstructure in block copolymer−water−"oil" systems by varying the copolymer composition and the "oil" type: small-angle X-ray scattering and deuterium-NMR investigation, J. Phys. Chem. B 102 (7) (1998) 1149–1158.
[16] R. Ivanova, B. Lindman, P. Alexandridis, Modification of the lyotropic liquid crystalline microstructure of amphiphilic block copolymers in the presence of cosolvents, Adv. Colloid Interface Sci. 89-90 (2001) 351–382.
[17] R. Rajabalaya, M.N. Musa, N. Kifli, S.R. David, Oral and transdermal drug delivery systems: role of lipid-based lyotropic liquid crystals, Drug Des. Devel Ther. 11 (2017) 393–406.
[18] A.K. Rajasekharan, R. Bordes, C. Sandstrom, M. Ekh, M. Andersson, Hierarchical and heterogeneous bioinspired composites-merging molecular self-assembly with additive manufacturing, Small 13 (28) (2017).
[19] N.S. Hmeidat, R.C. Pack, S.J. Talley, R.B. Moore, B.G. Compton, Mechanical anisotropy in polymer composites produced by material extrusion additive manufacturing, Addit. Manuf. 34 (2020), 101385.
[20] K. Sapouna, Y.P. Xiong, R.A. Shenoi, Dynamic mechanical properties of isotropic/anisotropic silicon magnetorheological elastomer composites, Smart Mater. Struct. 26 (11) (2017), 115010.
[21] J. Stasiak, J. Brubert, M. Serrani, S. Nair, F. de Gaetano, M.L. Costantino, G. D. Moggridge, A bio-inspired microstructure induced by slow injection moulding of cylindrical block copolymers, Soft Matter 10 (32) (2014) 6077–6086.
[22] A.K. Rajasekharan, M. Andersson, Role of nanoscale confinement on calcium phosphate formation at high supersaturation, Cryst. Growth Des. 15 (6) (2015) 2775–2780.
[23] V. Lutz-Bueno, J. Zhao, R. Mezzenga, T. Pfohl, P. Fischer, M. Liebi, Scanning-SAXS of microfluidic flows: nanostructural mapping of soft matter, Lab Chip 16 (20) (2016) 4028–4035.

[24] N.P. Balsara, D. Perahia, C.R. Safinya, M. Tirrell, T.P. Lodge, Birefringence detection of the order-to-disorder transition in block copolymer liquids, Macromolecules 25 (15) (1992) 3896–3901.
[25] J.J. Cardiel, H. Furusho, U. Skoglund, A.Q. Shen, Formation of crystal-like structures and branched networks from nonionic spherical micelles, Sci. Rep. 5 (1) (2015) 17941.
[26] F. Nallet, P. Barois, Anomalous birefringence of swollen lamellar phases: blue smectics, J. De. Phys. II 4 (6) (1994) 1049–1060.
[27] G. Schmidt, S. Müller, P. Lindner, C. Schmidt, W. Richtering, Shear orientation of lyotropic hexagonal phases, J. Phys. Chem. B 102 (3) (1998) 507–513.
[28] Y. Yang, X. Song, X. Li, Z. Chen, C. Zhou, Q. Zhou, Y. Chen, Recent progress in biomimetic additive manufacturing technology: from materials to functional structures, Adv. Mater. 30 (36) (2018), 1706539.
[29] G. Siqueira, D. Kokkinis, R. Libanori, M.K. Hausmann, A.S. Gladman, A. Neels, P. Tingaut, T. Zimmermann, J.A. Lewis, A.R. Studart, Cellulose nanocrystal inks for 3D printing of textured cellular architectures, Adv. Funct. Mater. 27 (12) (2017), 1604619.
[30] N.A. Sather, H. Sai, I.R. Sasselli, K. Sato, W. Ji, C.V. Synatschke, R.T. Zambrotta, J. F. Edelbrock, R.R. Kohlmeyer, J.O. Hardin, J.D. Berrigan, M.F. Durstock, P. Mirau, S.I. Stupp, 3D printing of supramolecular polymer hydrogels with hierarchical structure, Small 17 (5) (2021), 2005743.
[31] A.J. Hess, A.J. Funk, Q. Liu, J.A. De La Cruz, G.H. Sheetah, B. Fleury, I.I. Smalyukh, Plasmonic metamaterial gels with spatially patterned orientational order via 3D printing, ACS Omega 4 (24) (2019) 20558–20563.
[32] P. Kraft, A. Bergamaschi, C. Broennimann, R. Dinapoli, E.F. Eikenberry, B. Henrich, I. Johnson, A. Mozzanica, C.M. Schleputz, P.R. Willmott, B. Schmitt, Performance of single-photon-counting PILATUS detector modules, J. Synchrotron Radiat. 16 (Pt 3) (2009) 368–375.
[33] M. van Gurp, The use of rotation matrices in the mathematical description of molecular orientations in polymers, Colloid Polym. Sci. 273 (7) (1995) 607–625.
[34] J. Yu, F. Tian, S. Chen, X. Wang, Y. Zhang, H. Wang, Structure and property development of aromatic copolysulfonamide fibers during wet spinning process, J. Appl. Polym. Sci. 132 (31) (2015) n/a.
[35] N. Shane, F. John, A. Oriol, K. Bart, Imaging with photoelastic modulators, Proc. SPIE, 2014.
[36] C.-Y. Han, Y.-F. Chao, Photoelastic modulated imaging ellipsometry by stroboscopic illumination technique, Rev. Sci. Instrum. 77 (2) (2006), 023107.
[37] A. Rodriguez-Palomo, V. Lutz-Bueno, X. Cao, R. Kádár, M. Andersson, M. Liebi, In situ visualization of the structural evolution and alignment of lyotropic liquid crystals in confined flow, Small 17 (2021), 2006229.
[38] S.P. Meeker, R.T. Bonnecaze, M. Cloitre, Slip and flow in pastes of soft particles: direct observation and rheology, J. Rheol. 48 (6) (2004) 1295–1320.
[39] M. Cloitre, R.T. Bonnecaze, A review on wall slip in high solid dispersions, Rheol. Acta 56 (3) (2017) 283–305.
[40] M.M. Denn, Extrusion instabilities and wall slip, Annu. Rev. Fluid Mech. 33 (1) (2001) 265–287.
[41] H.S. Tang, D.M. Kalyon, Time-dependent tube flow of compressible suspensions subject to pressure dependent wall slip: Ramifications on development of flow instabilities, J. Rheol. 52 (5) (2008) 1069–1090.
[42] X. Yang, S.-Q. Wang, C. Chai, Extrudate swell behavior of polyethylenes: capillary flow, wall slip, entry/exit effects and low-temperature anomalies, J. Rheol. 42 (5) (1998) 1075–1094.
[43] C. Ge, Y. Wu, J. Xu, Stability and optimum polymerized condition of polysiloxane–polyacrylate core/shell polymer, Adv. Polym. Technol. 29 (3) (2010) 161–172.
[44] J.A. Lewis, Direct ink writing of 3D functional materials, Adv. Funct. Mater. 16 (17) (2006) 2193–2204.
[45] J.J. Cardiel, D. Takagi, H.-F. Tsai, A.Q. Shen, Formation and flow behavior of micellar membranes in a T-shaped microchannel, Soft Matter 12 (39) (2016) 8226–8234.
[46] J. Emmermacher, D. Spura, J. Cziommer, D. Kilian, T. Wollborn, U. Fritsching, J. Steingroewer, T. Walther, M. Gelinsky, A. Lode, Engineering considerations on extrusion-based bioprinting: interactions of material behavior, mechanical forces and cells in the printing needle, Biofabrication 12 (2) (2020), 025022.
[47] O. Diat, D. Roux, F. Nallet, Effect of shear on a lyotropic lamellar phase, J. Phys. II Fr. 3 (9) (1993) 1427–1452.
[48] B. Sarkar, J. Lakshmichand, P. Alexandridis, Self-assembly of amphiphilic block copolymers in ternary solvent mixtures: lyotropic liquid crystalline phase behavior and structure, Macromol. Chem. Phys. 213 (23) (2012) 2514–2528.
[49] B. Svensson, P. Alexandridis, U. Olsson, Self-assembly of a poly(ethylene oxide)/poly(propylene oxide) block copolymer (Pluronic P104, (EO)27(PO)61(EO)27) in the presence of water and xylene, J. Phys. Chem. B 102 (39) (1998) 7541–7548.